https://doi.org/10.5194/egusphere-2025-4367
Preprint. Discussion started: 23 September 2025

Impact of the Indian Ocean Sea Surface Temperature on the Southern Hemisphere Middle Atmosphere

Chengyun Yang[1,2,3], Xiang Guo[1], Tao Li[1,2,3*], Xinyue Wang[4], Jun Zhang[5], Xin Fang[1,2,3] and Xianghui Xue[1,2,3]

[1] School of Earth and Space Sciences, University of Science and Technology of China, Hefei, 230026, China

[2] CAS Center for Excellence in Comparative Planetology/CAS Key Laboratory of Geospace Environment/Mengcheng National Geophysical Observatory, University of Science and Technology of China, Hefei 230026, China

[3] Hefei National Laboratory, University of Science and Technology of China, Hefei 230088. China

[4] Department of Atmospheric and Oceanic Sciences, University of Colorado, Boulder, U.S.

[5] Atmospheric Chemistry Observations & Modeling Laboratory, NSF National Center for Atmospheric Research

Correspondence to: Tao Li (litao@ustc.edu.cn)

Abstract.

An index representing the midlatitude Indian Ocean Dipole (MIOD) is derived from the second empirical orthogonal function (EOF) mode of austral winter (JJA) sea surface temperature (SST) anomalies to examine its impact on the Southern Hemisphere middle and upper atmosphere. ERA5 reanalysis datasets, together with satellite observations and WACCM6 simulations, are used to analyze the associated atmospheric responses to MIOD. The results show pronounced but asymmetric impacts between positive and negative events, primarily driven by differences in wavenumber-1 planetary wave activity. Positive MIOD events enhance planetary-wave propagation from the Indian Ocean sector, leading to momentum deposition, variations in temperature, zonal winds, as well as a strengthening of the residual meridional circulation. These dynamical anomalies warm the midlatitude stratosphere, modify the polar vortex morphology, and redistribute ozone in the midlatitudes. Changes in stratospheric winds

https://doi.org/10.5194/egusphere-2025-4367
Preprint. Discussion started: 23 September 2025

further regulate gravity-wave filtering, providing a pathway for SST signals to extend upward into the mesosphere. In contrast, negative events generally produce weaker and less statistically robust signals. These findings highlight the importance of incorporating Indian Ocean variability into stratospheric and climate modeling to improve understanding of atmosphere–ocean coupling mechanisms and their implications for polar climate change.

1 Introduction

The stratosphere plays a crucial role in atmospheric vertical coupling and in shaping the evolution of the climate system, through both radiative and dynamical processes that connect it to the troposphere and influence global climate variability. Stratospheric thermal radiation is suggested to have significant influences on both tropical and extratropical circulation, with further effects on surface temperature **(Joshi et al., 2006; Maycock et al., 2013; Shindell, 2001; Solomon et al., 2010; Tandon et al., 2011)**. Dynamically, extratropical stratospheric anomalies, particularly variations in the polar vortex, can propagate downward within 1–2 months and significantly disturb tropospheric circulation **(Baldwin and Dunkerton, 2001; Limpasuvan et al., 2005; Mitchell et al., 1999)**.

In the Southern Hemisphere (SH), such stratospheric disturbances play an especially prominent role in vertical coupling across the troposphere, stratosphere, and mesosphere, while also interacting with the tropospheric climate system. For instance, the major SSW events in the SH during the 21st century triggered vertically coupled atmospheric responses dominated by wave–mean flow interaction dynamics **(Dowdy et al., 2004; Mbatha et al., 2010; Yang et al., 2022)**. The variation in the troposphere and lower stratosphere can also affect the upper atmosphere through modulating wave-mean flow interaction **(Black and McDaniel, 2007; García-Herrera et al., 2006; Li et al., 2013, 2016a; Yang et al., 2017; Karlsson et al., 2011; Lindzen, 1981)**.

In addition to internally generated variability, external forcing from the ocean also exert important influences on stratospheric processes. Tropical sea surface temperature (SST) variations, particularly those associated with ENSO, are known to influence stratospheric processes through both water vapor transport and dynamical pathways such as Rossby wave propagation **(Domeisen et al., 2019; Garfinkel et al., 2013, 2021; Li et al., 2016a; Yang et al., 2015)**. Beyond the tropical Pacific Ocean, SST anomalies in other ocean basins—including the

https://doi.org/10.5194/egusphere-2025-4367
Preprint. Discussion started: 23 September 2025

Indian and Atlantic Oceans-have also been shown to affect the stratosphere **(Xie et al., 2018; Zhou et al., 2018)**. For example, variability in the Indo-Pacific warm pool has been associated with changes in lower stratospheric humidity, with warming leading to drying and cooling to moistening **(Xie et al., 2018)**. Long-term warming of the Atlantic Ocean has contributed to the observed increase in stratospheric water vapor over the past century **(Xie et al., 2020)** and can affect stratospheric circulation at mid- and high latitudes by inducing atmospheric teleconnections and modulating planetary wave propagation **(Rao and Ren, 2018)**.

Among these oceanic influences, variability within the tropical Indian Ocean has distinct internal modes that significantly modulate tropospheric and stratospheric circulation. The Indian Ocean Basin Mode (IOBM), characterized by basin-wide SST warming, affects precipitation in the troposphere **(Xie et al., 2009)** and influences the stratosphere by altering planetary wave propagation **(Rao and Ren, 2016; Li et al., 2016b)** and the strength and position of the polar vortex **(Rao and Ren, 2020)**. It has also been linked to the Northern Annular Mode (NAM) response that can offset the effects of tropical Pacific SST anomalies **(Fletcher and Kushner, 2011)**. The Indian Ocean Dipole (IOD), defined by a zonal SST gradient, influences regional and remote climate by modulating large-scale circulations and rainfall variability **(Ashok et al., 2001; Guan and Yamagata, 2003; Ramsay et al., 2017; Saji et al., 1999; Tozuka et al., 2016)**. Beyond its tropospheric impacts, the IOD has also been identified as a driver of Southern Hemisphere climate variability and may affect the stratosphere through the excitation of extratropical wave trains and modulation of wave propagation **(Saji and Yamagata, 2003; Risbey et al., 2009; Son et al., 2013; Rao et al., 2020)**. Strong IOD events in particular have been linked to persistent annular mode responses and stratospheric teleconnections **(Fletcher and Cassou, 2015; Bègue et al., 2010)**.

While extensive efforts have been made to understand the impacts of tropical Indian Ocean variability-including both basin-wide warming (IOBM) and zonal SST gradients (IOD)-on tropospheric and stratospheric circulation, relatively little attention has been given to SST anomalies outside the tropical region. Distinctive SST variability modes also exist in the extratropical Southern Hemisphere Indian Ocean, including the Subtropical Indian Ocean Dipole (SIOD) **(Behera et al., 2000; Swadhin and Yamagata, 2001)** and Ningaloo Niño **(Ryan et al., 2021)**, each characterized by unique spatial and temporal patterns. However, the influence of these subtropical Indian Ocean SST indices on the middle and upper atmosphere remains largely

https://doi.org/10.5194/egusphere-2025-4367
Preprint. Discussion started: 23 September 2025

unexplored, despite their potential importance in modulating stratospheric dynamics through planetary wave excitations.

Considering the substantial hemispheric asymmetry in ocean coverage-the SH is significantly more ocean-dominated (81%) compared to the Northern Hemisphere (NH, 61%) **(Smith and Sandwell, 1997)**, planetary wave activity in the Southern Hemisphere is predominantly influenced by oceanic thermal forcing rather than orographic effects **(Brayshaw et al., 2008; Held et al., 2002)**. Over 90% of the net increase in global ocean heat content in recent decades has occurred in the Southern Hemisphere **(Rathore et al., 2020)**, highlighting the growing climatic influence of Southern Hemisphere oceanic processes. These considerations raise the possibility that SST variability over the subtropical to midlatitude Indian Ocean may exert a more direct and underappreciated influence on stratospheric circulation via modulation of planetary wave activity.

Since conventional Indian Ocean SST indices predominantly represent SST variability peaking during austral summer, coincident with the peak of ENSO, their utility in characterizing the austral winter ocean–atmosphere coupling remains limited. Yet the atmospheric background conditions during austral winter are more favorable for planetary wave propagation into the stratosphere, thereby promoting vertical atmospheric coupling. Considering recent changes in the spatiotemporal characteristics of Indian Ocean SST anomalies under climate change, this study aims to re-examine the wintertime SST variability from the tropical to midlatitude Indian Ocean during the Austral wintertime (June-July-August, JJA) and investigate its impacts on the Southern Hemisphere stratosphere and higher atmospheric layers. The remainder of this paper is organized as follows. Section 2 describes the datasets, model simulations, and analysis methods used in this study. Section 3 presents the identification of the SST variability modes, the definition of event years, and the associated stratospheric responses. Section 4 examines how the influences extend further into the mesosphere, analyzing the relevant dynamical processes and discussing their implications for the interpretation of the results. Section 5 provides a summary of the main findings.

2 Data and Method

2.1 Observations and simulations

Previous studies have shown that major Indian Ocean SST modes, such as the subtropical Indian dipole, typically peak during the Northern Hemisphere winter **(e.g. Behera et al., 2000;**

https://doi.org/10.5194/egusphere-2025-4367
Preprint. Discussion started: 23 September 2025

Swadhin and Yamagata, 2001). Considering the emerging spatiotemporal changes in Indian Ocean SST patterns under ongoing climate change (e.g., Tong et al., 2025), we re-evaluate the dominant variability of Indian Ocean SST anomalies during the austral winter (June–August) using Empirical Orthogonal Function (EOF) analysis. The Hadley Centre Sea Ice and Sea Surface Temperature (HadISST) dataset, developed by the UK Met Office, was used to analyze the spatiotemporal characteristics of SST variability over the midlatitudes of the Indian Ocean (Rayner et al., 2003). HadISST provides a long-term, globally complete record of sea surface temperature and sea ice concentration based on merged observations from ships, buoys, and satellites, with quality control and homogenization applied. Monthly fields at 1°×1° resolution were used for 1980–2022, from which June–August (JJA) means were calculated for analysis.

To investigate the atmospheric response to the SST anomalies, this study uses atmospheric temperature, wind, and geopotential height (hgt) data from the European Centre for Medium-Range Weather Forecasts (ECMWF) Reanalysis v5 (ERA5). ERA5 is the fifth-generation global reanalysis dataset developed by ECMWF, produced using advanced data assimilation techniques and the IFS Cy41r2 forecasting model (Hersbach et al., 2020). It combines a wide range of observations, including satellite, radiosonde, and surface station data, to provide high-resolution, spatiotemporally continuous climate fields. The variables used in this study are daily means for the period 1979-2022, extracted at 1° × 1° horizontal resolution on 37 standard pressure levels extending up to 1 hPa (~50 km), providing adequate coverage of the stratosphere.

This study also uses temperature observations from the SABER and Halogen Occultation Experiment (HALOE) satellite instruments (Russell et al., 1993). The HALOE onboard the Upper Atmosphere Research Satellite (UARS), operated from October 1991 to November 2005 as part of NASA's Mission to Planet Earth. HALOE retrieved vertical profiles of temperature and several trace gases (e.g., O_3, HCl) by solar occultation, using multiple infrared channels. Temperature profiles in the middle atmosphere (~40-80 km) were derived from CO_2 absorption near 2.8 μm, with a vertical resolution of approximately 4 km and an accuracy of ~5 K below 80 km. HALOE provided daily sunrise and sunset observations within ±50° latitude, though data are sparse in the summer hemisphere.

The Sounding of the Atmosphere using Broadband Emission Radiometry (SABER) instrument aboard NASA's Thermosphere Ionosphere Mesosphere Energetics and Dynamics (TIMED) satellite has been operating since December 2001 (Russell et al., 1999). It alternates between northern (52°S–83°N) and southern (83°S–52°N) hemisphere viewing modes, providing

https://doi.org/10.5194/egusphere-2025-4367
Preprint. Discussion started: 23 September 2025

full local time coverage approximately every 60 days. SABER measures limb radiance in the 15 μm CO_2 band to retrieve vertical temperature profiles from ~10 to 120 km, covering the stratosphere, mesosphere, and lower thermosphere. The vertical resolution is ~2 km, with an accuracy better than 2 K in the stratosphere and mesosphere. The SABER Version 2.0 temperature dataset offers long-term, high-quality observations widely used for studying atmospheric waves and variability.

Simulations from the Specified Dynamics configuration of Whole Atmosphere Community Climate Model version 6 (WACCM6-SD) were used to examine the upper atmospheric response to Indian Ocean SST anomalies. WACCM6 is a high-top atmospheric model developed at NCAR as part of CESM2, with comprehensive physical and chemical processes extending from the surface to the lower thermosphere **(Gettelman et al., 2019)**. In the SD configuration, meteorological fields are nudged toward MERRA-2 reanalysis every six hours to reduce internal variability and model bias. The version used here was run at 0.95° × 1.25° horizontal resolution with 70 vertical levels and a model top near 140 km. It includes the TSMLT chemistry mechanism, and simulations were conducted for 1980–2022, constrained by historical SST and anthropogenic emissions from the Community Emissions Data System (CEDS).

A multi-source satellite ozone dataset from NASA's Goddard Space Flight Center was used to analyse Antarctic ozone conditions, including total column ozone, ozone hole area, and ozone mass deficit, covering the period from 1979 to the present **(Van Der A et al., 2010)**. The dataset integrates observations from multiple satellite instruments: TOMS onboard Nimbus-7 (1979–1992), TOMS on Meteor-3 (1993–1994), Earth Probe TOMS (1996–October 2004), OMI on Aura (November 2004–June 2016), and OMPS on Suomi NPP (since July 2016), with additional correction and gap-filling using MERRA-2 and GEOS FP data.

2.2 Analysis method

To obtain a longer-term record of upper atmospheric temperature, monthly mean data from HALOE and SABER were merged to generate a continuous dataset spanning the period from 1991 to 2020. Temperature profiles from both instruments were first interpolated onto a uniform grid with 1-km vertical spacing between 40 and 80 kilometers, and 5° latitude intervals between 55°S and 55°N. For HALOE, daily sunrise and sunset profiles were first averaged separately by month, then combined to reduce diurnal tide influences. For SABER, ascending and descending profiles were first averaged daily, and then a two-month running mean was applied to further suppress tidal signals. Due to differences in sampling characteristics, SABER more effectively

https://doi.org/10.5194/egusphere-2025-4367
Preprint. Discussion started: 23 September 2025

removes semidiurnal tides, while residual tidal contamination may remain in HALOE monthly means, potentially introducing temperature biases. To construct a unified temperature dataset, HALOE and SABER monthly mean profiles were first bias-corrected based on their mean differences during the overlap period. A constant offset was applied to each dataset to minimize discontinuities, ensuring consistency in the merged time series. The corrected HALOE and SABER records were then concatenated to produce a continuous monthly temperature dataset for the period 1991-2020, following the method described by **Li et al. (2021)**.

Since middle and upper atmospheric variability is influenced by external drivers such as solar activity and the quasi-biennial oscillation (QBO) **(Li et al., 2013)**, a multiple linear regression (MLR) approach was applied to remove their linear effects and long-term trends, thereby isolating the response to Indian Ocean SST anomalies. Following the method of **Li et al. (2016)**, monthly anomalies were calculated by subtracting the multi-year monthly climatology from the original data to eliminate the seasonal cycle. The resulting anomalies were then regressed onto several external drivers, including El Niño–Southern Oscillation (ENSO), the QBO, the equivalent effective stratospheric chlorine (EESC), and the 11-year solar cycle. ENSO was represented by the Niño 3.4 index, defined as the 3-month running mean of SST anomalies averaged over 5°N–5°S and 120°–170°W. QBO was captured using two orthogonal predictors: the equatorial zonal-mean zonal wind at 10 hPa (QBO10) and 30 hPa (QBO30) derived from ERA5 reanalysis datasets. The equivalent effective stratospheric chlorine time series used in this study corresponds to the WMO A1-2010 scenario and uses the method suggested by **(Newman et al., 2007)**. 11 year solar activity was represented by the 10.7 cm solar radio flux (F10.7), which serves as a proxy for solar ultraviolet (UV) variability and has been continuously monitored since 1947 by Canadian agencies.

The multiple linear regression model is expressed as follows:

$$T(t)=\alpha\cdot NINO3.4+\beta1\cdot QBO10+\beta2\cdot QBO30+\gamma\cdot F10.7+\delta\cdot EESC+\kappa\cdot trend+\varepsilon \quad (1)$$

where *T(t)* denotes the monthly anomaly of the target atmospheric variable, the term trend represents the long-term linear trend, and ε is the regression residual, i.e., the atmospheric component with the influence of unrelated factors removed. The coefficients α, $\beta1$, $\beta2$, γ and δ correspond to the contributions from ENSO, QBO at 10 hPa and 30 hPa, 11-yr solar cycle and EESC, respectively.

Given the limited number of events, the Monte Carlo method was employed to assess the statistical significance of the composite results in this work. Specifically, 1,000 synthetic

https://doi.org/10.5194/egusphere-2025-4367
Preprint. Discussion started: 23 September 2025

composites were generated by randomly selecting the same number of years as the target events (without replacement) from the whole time period, assuming a null hypothesis that the composite signal arises purely from internal variability. For each realization, the composite was recalculated to build an empirical distribution. Two-sided significance thresholds were then determined based on the 2.5th and 97.5th percentiles of this distribution (corresponding to a 95% confidence level). If the actual composite value falls outside this range, the null hypothesis is rejected and the result is considered statistically significant.

To quantify the influence of planetary wave-induced momentum and heat fluxes on the zonal-mean circulation, the Eliassen-Palm (E-P) flux and its divergence were calculated following the formulation of **(Andrews et al., 1987)**. The meridional and vertical components of the E-P flux in pressure coordinates are given by:

$$F_y = \rho_0 a \cos\varphi \left(-[u'v'] + \frac{[u]_z [v'\theta']}{[\theta_z]} \right), \quad (2)$$

$$F_z = \rho_0 \, \mathrm{acos}\,\varphi \left(\left[\mathrm{f} - \frac{(\bar{u}\cos\varphi)_\varphi}{a\cos\varphi} \right] \frac{[v'\theta']}{[\theta_z]} - [u'w'] \right), \quad (3)$$

$$\mathrm{Div} = \frac{1}{\mathrm{acos}\,\varphi} \frac{\partial \left(F_y \cos\varphi \right)}{\partial \varphi} + \frac{\partial F_z}{\partial z}. \quad (4)$$

where ρ_0 denotes air density, a is the Earth's radius, φ is latitude, and f is the Coriolis parameter. The variables u', v', w', and θ' represent the zonal anomalies of zonal wind, meridional wind, vertical velocity, and potential temperature associated with planetary waves, respectively. Square brackets indicate the zonal mean.

To separate wave-induced disturbances from the mean circulation, the residual mean meridional circulation was derived based on the transformed Eulerian mean (TEM) framework proposed by **(Andrews and McIntyre, 1976)**. By incorporating corrections from the eddy heat flux ($[v'\theta']$), this approach provides a clearer depiction of wave–mean flow interactions. The residual circulation components are given by:

$$v^* = [v] - \frac{1}{\rho_0} \frac{\partial}{\partial z} \left(\frac{[v'\theta']}{\partial \bar{\theta}/\partial z} \right) \quad (4)$$

$$w^* = [w] + \frac{1}{a\cos\phi} \frac{\partial}{\partial \phi} \left(\frac{\cos\phi [v'\theta']}{\partial [\theta]/\partial z} \right) \quad (5)$$

2.3 Middle latitude Indian Dipole events

https://doi.org/10.5194/egusphere-2025-4367
Preprint. Discussion started: 23 September 2025

To focus on year-to-year variability rather than long-term climate trends, the JJA-mean SST time series at each grid point was linearly detrended. To further account for the influence of long-term stratospheric ozone changes, the EESC index was regressed out using multiple linear regression. EESC represents a combined metric of ozone-depleting substances (ODS), such as chlorofluorocarbons (CFCs), and is commonly used to assess the impact of halogen loading on stratospheric ozone depletion and recovery. The EESC data used in this study were obtained from the Scientific Assessment of Ozone Depletion: 2022 report published by the UNEP Ozone Secretariat, which provides both historical estimates (from 1980 onward) and future projections. The detrending and EESC adjustment were implemented via the following multiple-linear-regression equation:

$$SST\_residual(t) = SST(t) - \beta_1 \cdot t - \beta_2 \cdot EESC(t). \quad (9)$$

where β_1 and β_2 are regression coefficients associated with the long-term linear trend and the EESC index, respectively. Then, the JJA-mean SST at each grid point was normalized by subtracting its temporal mean and dividing by the standard deviation, to suppress regional variability magnitude and emphasize spatial anomaly structures in the EOF analysis.

An EOF analysis was applied to the detrended and standardized JJA-mean SST over the Indian Ocean region (60°S–5°N, 40°E–145°E), yielding the leading two modes of SST variability during austral winter, as shown in **Fig. 1**. EOF1 and EOF2 explains 16% and 13.6 % of the total variance of the normalized Indian Ocean SST anomalies. The first mode (EOF1) is characterized by coherent SST anomalies over the tropical Indian Ocean, extending southward into the midlatitudes. Notably, opposite anomalies appear in the midlatitude regions near 40°E–60°E and around 140°E at approximately 45°S. This mode explains 16 % of the total variance. The second mode (EOF2) shows a dipole-like pattern, featuring opposite SST anomalies between the region off the west coast of Australia extending into the northeastern tropical Indian Ocean, and the central midlatitude Indian Ocean located around 40°S, 70°E. This spatial pattern bears some resemblance to the subtropical Indian Ocean dipole (SIOD), but with a more eastward-displaced structure overall. The difference between the JJA EOF2 SSTA pattern and the SIOD pattern may arise from the Indian Ocean response to climate change **(e.g. Sun et al., 2022)**. Notably, the JJA-mean SIOD index, calculated using its traditional definition **(Swadhin and Yamagata, 2001)**, shows a moderate correlation with the PC2 at 0.54. However, distinct differences remain, possibly because the EOF2 pattern is derived solely from JJA SST anomalies and may also reflect evolving spatiotemporal SST characteristics in the Indian Ocean under recent climate change.

https://doi.org/10.5194/egusphere-2025-4367
Preprint. Discussion started: 23 September 2025

To better capture the year-to-year spatiotemporal variability of Indian Ocean SST during austral winter revealed by the EOF analysis, a new SST index was constructed. This index reflects the SST dipole pattern associated with PC2 and is defined as the difference between the area-averaged SST over the eastern margin of the subtropical Indian Ocean (100°–120°E, 5°–40°S) and the central midlatitude Indian Ocean (55°–90°E, 30°–45°S), as indicated by the rectangles in **Fig. 1b**. Using this physically based index rather than PC2 directly provides a simpler and more intuitive metric for subsequent analysis. A positive phase of this index corresponds to a pattern characterized by warming in the north-eastern sector and cooling in the central midlatitudes. Since this index reflects the SST gradient between the midlatitudes and the eastern part of the basin, it is referred to here as the Middle-latitude Indian Ocean Dipole (MIOD). As shown in **Fig. 2a**, the temporal evolution of the MIOD index closely tracks that of the second EOF principal component (PC2), with a correlation coefficient of 0.94.

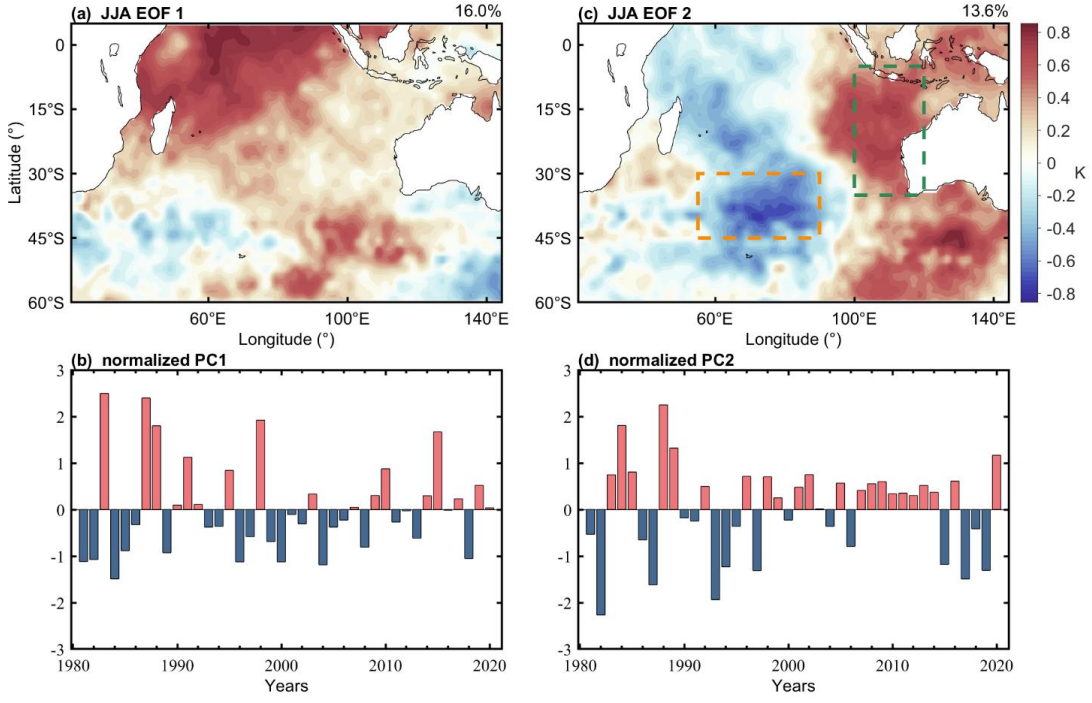

Figure 1. SST patterns of (a) EOF1 and (b) EOF2, and principal component time series of (c) EOF1 and (d) EOF2, derived from Indian Ocean SST anomalies during austral winter (JJA) for 1980–2020 over the domain 60°S–5°N, 40°E–145°E.

https://doi.org/10.5194/egusphere-2025-4367
Preprint. Discussion started: 23 September 2025

Based on the standard deviation of the austral winter (June–August) mean MIOD index, years with values exceeding +1.0 standard deviation were defined as positive MIOD events, while those below –1.0 standard deviation were defined as negative events. Although this SST pattern is not significantly correlated with ENSO, the correlation between the MIOD index and the Niño 3.4 index is only 0.27, some MIOD events still coincided with ENSO occurrences. To ensure the independence of the analyzed samples, ENSO events were identified using the Niño 3.4 index, with a threshold of ±1.0 standard deviation during June–August, and their temporal and spatial overlap, defined as ENSO and MIOD events occurring in the same year, is shown in **Fig. 2b**. After excluding overlapping cases, a set of independent MIOD anomaly events was selected, comprising five positive events (1984, 1992, 2002, 2005, and 2016) and seven negative events (1986, 1993, 1994, 2006, 2017, 2018, and 2019).

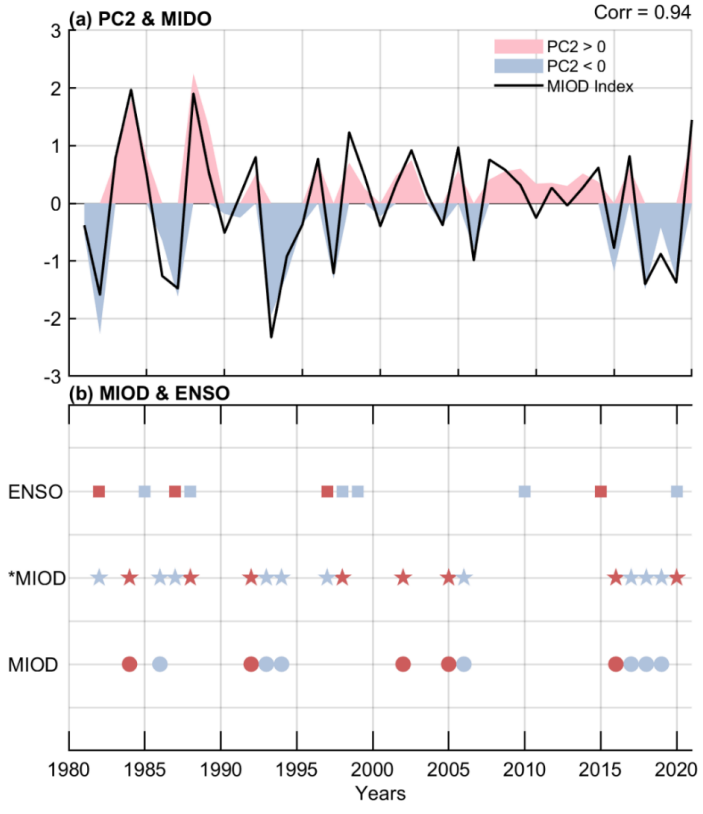

https://doi.org/10.5194/egusphere-2025-4367
Preprint. Discussion started: 23 September 2025

Figure 2: (a) Time series of the austral winter (June–August) mean MIOD index (solid line) and PC2 (colored bars). (b) Identification of MIOD anomaly events. Pentagrams denote the preliminary selection of MIOD events, squares indicate concurrent ENSO events, and circles mark the final set of independent MIOD events. Red and blue symbols represent independent positive and negative MIOD events, respectively.

3 Results

To investigate the impact of the MIOD on the Southern Hemisphere stratosphere, composite analyses of zonal-mean temperature and wind fields were performed based on the identified positive and negative MIOD events. **Fig. 3** presents the austral winter (JJA) stratospheric zonal-mean temperature anomalies associated with positive and negative MIOD events. The composites exhibit a pronounced asymmetry between positive and negative MIOD events. During positive MIOD events (**Fig. 3a** and **Fig. 3b**), a strong negative anomaly in zonal wind appears in the midlatitude stratosphere, centered near 38°S at the stratopause level (~1 hPa), with a minimum anomaly exceeding −18 m/s. In contrast, the high-latitude stratosphere exhibits significant positive wind anomalies, centered around 65°S with peak values reaching approximately +8.6 m/s. These zonal wind anomalies tilt poleward with decreasing altitude, as indicated by the zero-contour shifting from ~50°S near the stratopause (1 hPa) to ~70°S in the lower stratosphere (300 hPa). Over the equator, the upper and middle stratosphere exhibit a vertically alternating pattern, with negative anomalies (–10 m/s) near 3 hPa, positive anomalies (+2 m/s) around 10 hPa, and negative anomalies (~–6 m/s) near 50 hPa. Accompanying these wind changes, significant warming is observed in the Southern Hemisphere stratosphere, forming a “T-shaped” structure. The primary warming appears in the midlatitudes and near the stratopause. A broad region of positive temperature anomalies (> +1 K) extends throughout the stratosphere (300 hPa–1 hPa), intensifying with height and reaching a maximum of over +4 K near 3 hPa. The meridional extent also broadens from 45°S–60°S in the lower stratosphere to 30°S–70°S near the stratopause. Additionally, another warming center is detected near the South Pole at ~90°S and 3 hPa, with a peak of +4 K; however, no significant anomalies are present directly below this layer in the mid-stratosphere (> 3 hPa). For the negative MIOD events (**Fig. 3c** and **Fig. 3d**), the zonal-mean zonal wind and temperature anomalies are generally weak and fail to reach the 90% confidence level based on the Monte Carlo significance test.

https://doi.org/10.5194/egusphere-2025-4367
Preprint. Discussion started: 23 September 2025

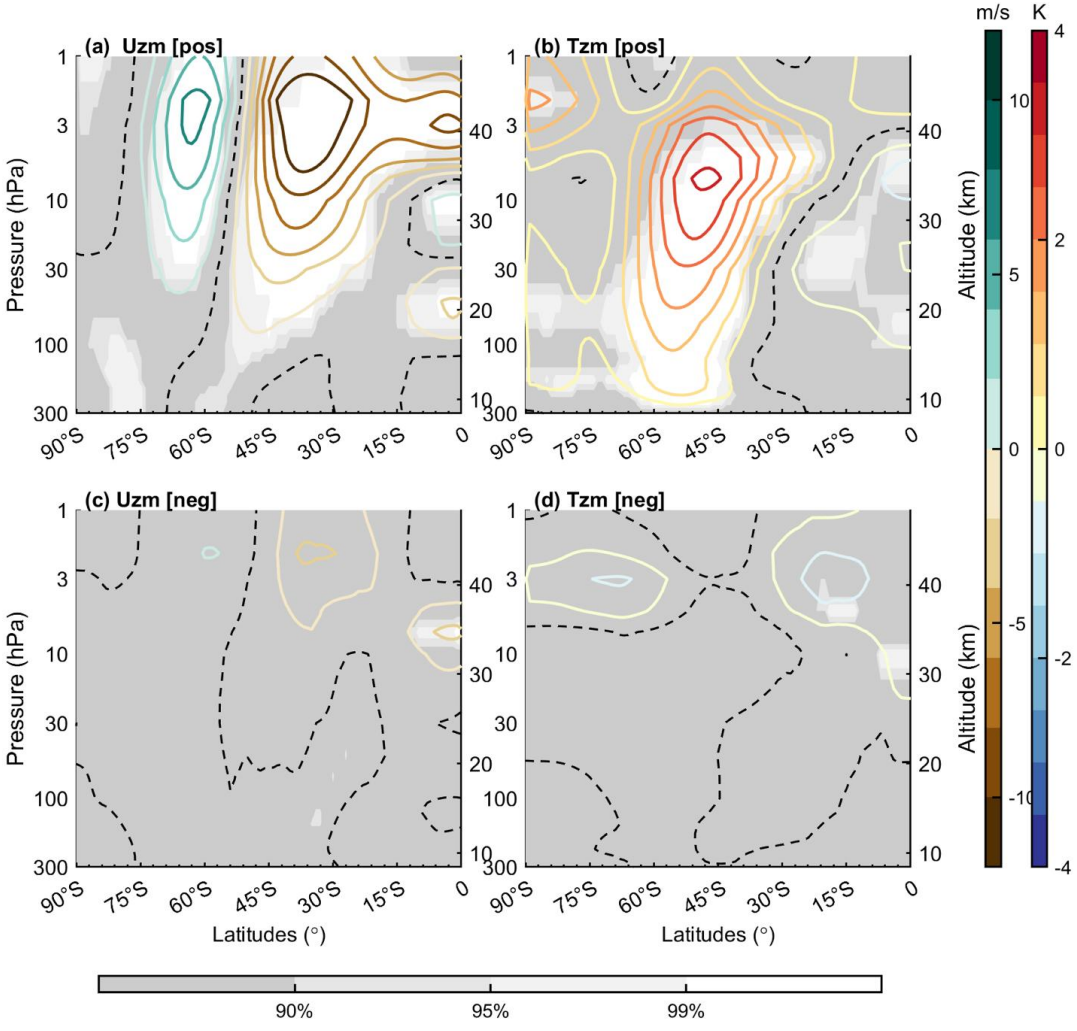

Figure 3: (a) Composite zonal-mean zonal wind anomalies for positive MIOD events. Contours represent wind anomalies, with the dashed contour denoting the zero line. Shading indicates statistically significant regions based on a Monte Carlo test. (b) Same as (a), but for the zonal mean temperature anomalies. (c) and (d), similar to (a) and (b) but for negative MIOD events.

This asymmetry between positive and negative events may reflect differences in SST characteristics and atmospheric response mechanisms associated with opposite phases of the MIOD. To explore this further, **Fig. 4** compares the spatial patterns of SST anomalies during positive and negative MIOD events. During positive-phase events (**Fig. 4a**), significant cold anomalies (~ –0.4 K) are centered over the midlatitude central Indian Ocean, extending southeastward from east of Madagascar (30°S, 60°E) to approximately 45°S, 100°E. Concurrent warm anomalies are confined to the vicinity of the Maritime Continent, with statistically

https://doi.org/10.5194/egusphere-2025-4367
Preprint. Discussion started: 23 September 2025

significant values limited to a small area. In contrast, positive-phase MIOD events (**Fig. 4b**) are characterized by a pronounced negative SST anomaly (–0.5 K) extending from south of the Maritime Continent toward the western coast of Australia, while warm anomalies are restricted to a relatively narrow region in the midlatitude central Indian Ocean.

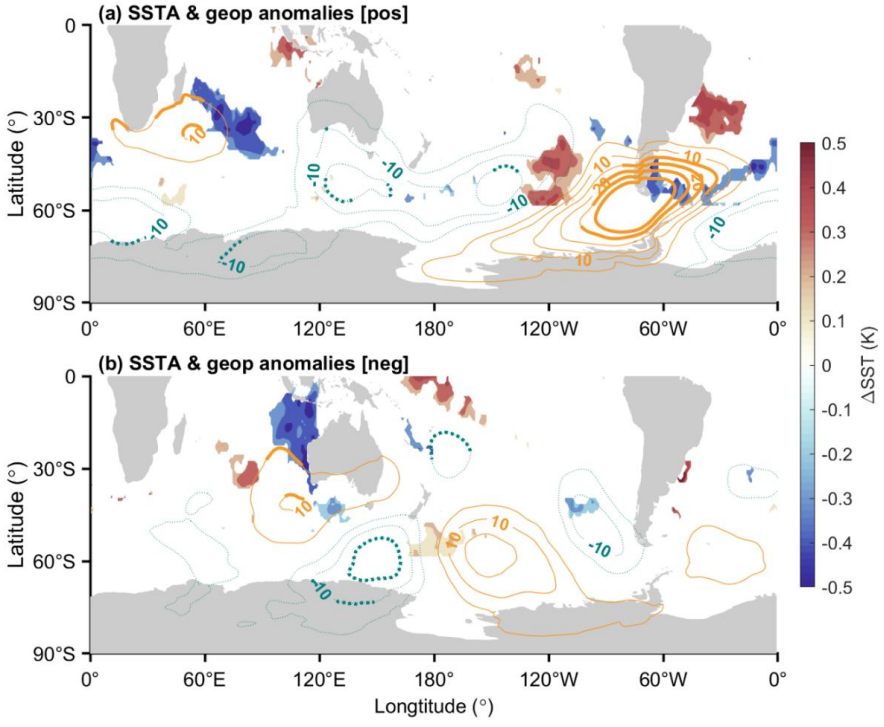

Figure 4: Composite anomalies for positive MIOD events during June–August (JJA). (a) Sea surface temperature (SST) anomalies (shading), with only regions passing the 90% Monte Carlo confidence test shown. Overlaid contours indicate zonal anomalous geopotential height at 850 hPa, with orange (blue) lines representing positive (negative) anomalies. Contours are bolded where the anomalies are statistically significant at the 90% confidence level. (b) is the same as (a) but for composite of negative events.

Given the ocean-dominated surface characteristics of the Southern Hemisphere, planetary wave activity is primarily modulated by thermal forcing associated with zonal SST anomalies and associated diabatic heating. Although both positive and negative phases of the MIOD are characterized by pronounced meridional SST gradients over the Indian Ocean, the asymmetry in their spatial distributions may lead to differences in the atmospheric wave response. Composite anomalies of the zonal deviation of 850 hPa hgt during the Southern Hemisphere winter (dashed and solid contours in **Fig. 4a**) indicate that, under positive MIOD conditions, a prominent

https://doi.org/10.5194/egusphere-2025-4367
Preprint. Discussion started: 23 September 2025

positive center (~+10 m) emerges over the western Indian Ocean to southern Africa (20°–60°E, 25°–45°S), west of the negative SST anomaly at the central Indian Ocean. Meanwhile, large areas of significant negative anomalies (–10 m) are observed over southern Australia and the southwestern Pacific (90°–140°E, 30°–55°S). Accompanied by a positive hgt anomaly over southern South America and a negative HGT center over the South Atlantic, the composite anomalies form a coherent meridional wave pattern extending across the Southern Hemisphere midlatitudes.

During negative MIOD events (**Fig. 4b**), a localized positive geopotential height anomaly (+13 m) is located over the southeastern Indian Ocean and the western coast of Australia (90–100°E, 25–45°S). The Southern Hemisphere midlatitudes near 60°S exhibit a triple wave pattern, characterized by negative, positive, and negative anomalies centered south of Australia (150°E), over the South Pacific (150°W), and off the west coast of South America (90°W), respectively (−15 m → +15 m → −10 m).

These results highlight a pronounced asymmetry in the 850 hPa geopotential height responses between positive and negative MIOD events. In particular, positive events are associated with a broader zonal gradient in geopotential height over the southern Indian Ocean, which likely facilitates the excitation of larger-scale and more coherent wave structures. Such large-scale wave activity may lead to stronger atmospheric responses and could help explain the differing circulation patterns associated with positive and negative MIOD events. To further diagnose the differences in planetary wave activity modulated by positive and negative MIOD events, a harmonic decomposition was performed on the 850 hPa geopotential height field. Based on zonal Fourier decomposition, the zonal anomalies of the geopotential height at each latitude were expanded and reconstructed to extract the planetary wave components corresponding to zonal wavenumbers 1-3 (WN-1, WN-2, WN-3). This approach allows us to isolate the dominant large-scale wave structures and examine their anomalies relative to the climatological mean, thereby assessing changes in wave phase alignment and amplitude associated with MIOD events.

For the dominant planetary wave component, zonal wavenumber 1 (WN-1), the composite anomalies show pronounced differences between positive and negative MIOD events. During positive events (**Fig. 5a**), strong WN-1 anomalies with amplitudes up to 18 m are excited at midlatitudes, exhibiting an in-phase structure with the climatological mean wave train. This phase alignment enhances the overall WN-1 amplitude by approximately 30%, indicating a

https://doi.org/10.5194/egusphere-2025-4367
Preprint. Discussion started: 23 September 2025

substantial reinforcement of the planetary wave. In contrast, during negative events (**Fig. 5d**), weaker WN-1 anomalies (~3 m) emerge over the midlatitudes (40°–60°S), results in a ~5% reduction in wave amplitude.

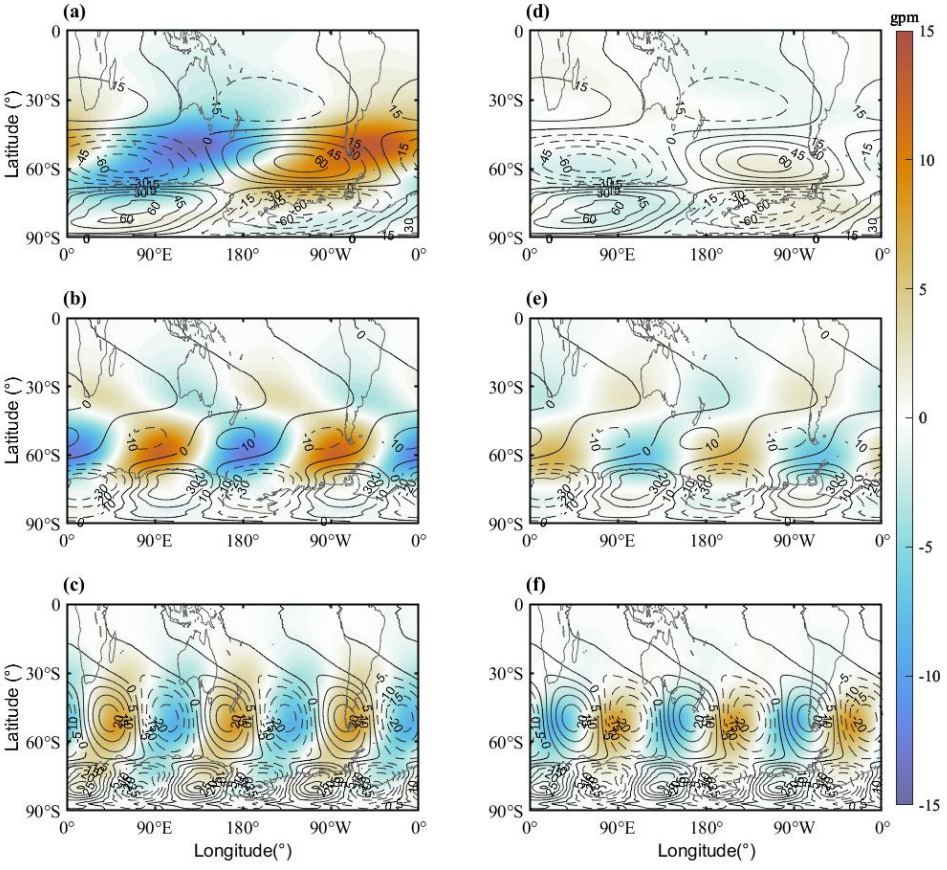

Figure 5: Composite anomalies of 850 hPa geopotential height for different zonal wavenumber planetary wave components during Southern Hemisphere winter (June–August, JJA), overlaid with the long-term climatological mean. (a–c) Composite results for positive MIOD events for zonal wavenumbers 1, 2, and 3, respectively; (d–f) same as (a–c), but for negative MIOD events. Shading indicates geopotential height anomalies, and contours represent the climatological mean.

The planetary wave with zonal wavenumber 2 (WN-2) exhibits distinct response characteristics (**Fig. 5b**). Under climatological conditions, the WN-2 amplitude at midlatitudes is relatively weak (~10 m). During positive MIOD events, a similar-magnitude anomaly (~12 m) is generated, but it is nearly out of phase (~180° phase shift) with the climatological wave,

https://doi.org/10.5194/egusphere-2025-4367
Preprint. Discussion started: 23 September 2025

substantially reducing the net WN-2 amplitude through destructive interference. Meanwhile, negative MIOD events generate WN-2 anomalies of comparable strength (~10 m), but with a phase structure approximately orthogonal (~90° phase shift) to the climatological pattern. As a result, the anomaly has limited projection onto the background wave and does not significantly alter the overall wave amplitude.

The planetary wave component with zonal wavenumber 3 (WN-3) also exhibits distinct responses between positive and negative MIOD events (**Fig. 5c and 5f**). In positive events, the WN-3 anomalies (~10 m) are nearly in phase with the climatological WN-3 pattern, resulting in constructive interference and a ~40% increase in wave amplitude. This reinforces the overall planetary wave activity. Similar to the WN-2 response, the WN-3 anomalies during negative MIOD events (~8 m) exhibit a phase structure that is approximately orthogonal to the climatological mean (~10 m). Consequently, the contribution of the anomaly to the background wave is limited, and the overall amplitude remains largely unchanged.

The differentiated responses of planetary waves with different zonal wavenumbers help explain the contrasting atmospheric responses of positive and negative MIOD events. Positive events, characterized by a unique SST anomaly structure, induce substantial zonal geopotential height gradients over the southern Indian Ocean, which effectively excite WN-1 and WN-3 components. This leads to enhanced planetary wave activity and a longer wave propagation path. On the other hand, negative events exert limited influence on WN-1 and primarily generate WN-2 and WN-3 anomalies that are nearly orthogonal to the climatological waves, resulting in minimal modulation of planetary wave amplitude.

To further assess how these wave responses modulate the vertical propagation of planetary waves, we examine the E–P flux and its divergence. **Fig. 6** presents the MIOD-related E-P flux anomalies during JJA. To better visualize the wave propagation from the lower troposphere to the upper stratosphere, a two-layer normalization approach is applied: the troposphere (900-300 hPa, **Fig. 6a**) and the stratosphere (300-1 hPa, **Fig. 6b**) are normalized separately, with F_{phi} and F_z in each layer divided by aπ and 10^5, respectively. The composite results reveal a clear enhancement of upward planetary wave propagation during positive MIOD events, consistent with the excitation of stronger WN-1 and WN-3 components.

https://doi.org/10.5194/egusphere-2025-4367
Preprint. Discussion started: 23 September 2025

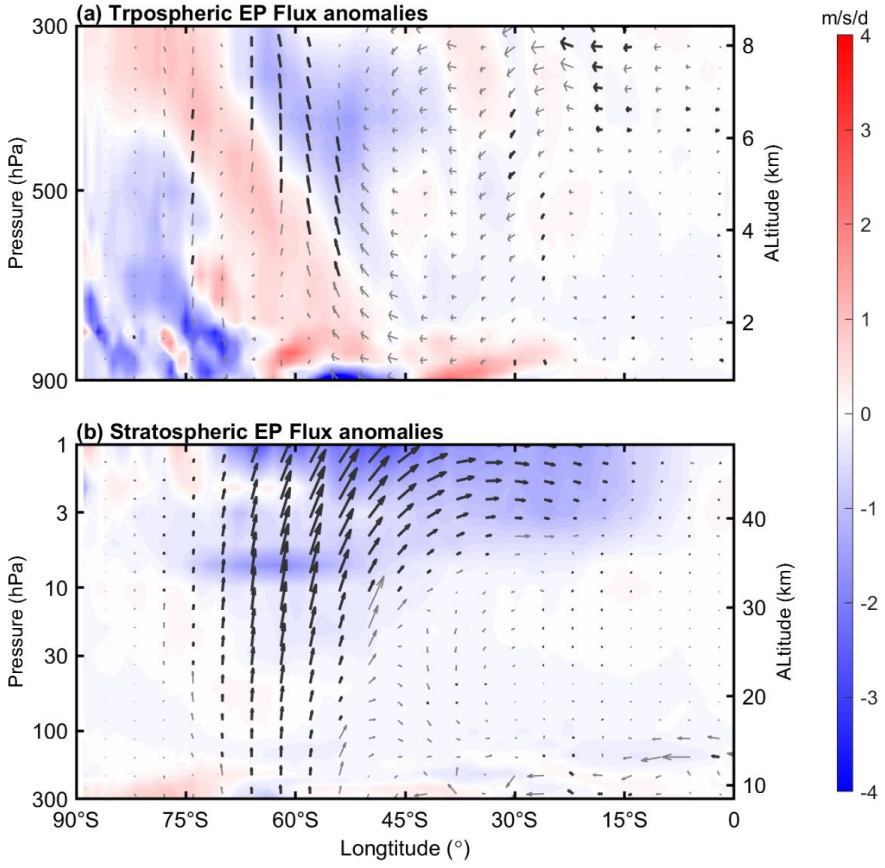

Figure 6: (a) Composite anomalies of tropospheric E–P flux components ($F\phi$, Fz) during positive MIOD events in June-August (JJA), with F_ϕ and F_z normalized by aπ and 10^6 respectively. Shading indicates the E-P flux divergence. Arrows denote the anomalous E-P flux vectors, with dark arrows marking vectors that pass the 90% Monte Carlo confidence test. (b) Same as (a), but for the stratosphere, with F_ϕ and F_z normalized by aπ and 10^5, respectively.

In the mid- to upper troposphere (**Fig. 6a**), significant anomalous upward propagation of planetary waves is observed over the midlatitudes (50°S-7°S). These regions of enhanced upward E-P flux coincide well with those identified in the lower stratosphere (**Fig. 6b**), indicating vertically coherent wave propagation. Above approximately 30 hPa, the upward-propagating wave activity begins to shift equatorward with height, and this meridional displacement becomes more pronounced at higher altitudes. Such latitudinal shifting of planetary wave propagation is likely modulated by the background waveguide structure of the Southern Hemisphere winter atmosphere **(Butchart et al., 1982)**. The upward- and equatorward-

https://doi.org/10.5194/egusphere-2025-4367
Preprint. Discussion started: 23 September 2025

propagating planetary waves in the stratosphere ultimately lead to a pronounced region of E-P flux divergence in the mid- to low-latitudes near the stratopause (1 hPa, 15°-55°S). This divergence indicates wave breaking and the deposition of westward momentum into the background flow, producing a peak deceleration anomaly of approximately −3 m s^{-1} day^{-1} - an enhancement of about 55% relative to the climatological mean (−5.6 m s^{-1} day^{-1}). This anomalous momentum forcing provides a dynamical explanation for the strong negative zonal wind center (~−18 m s^{-1}) observed in the midlatitude upper stratosphere in **Fig. 3**.

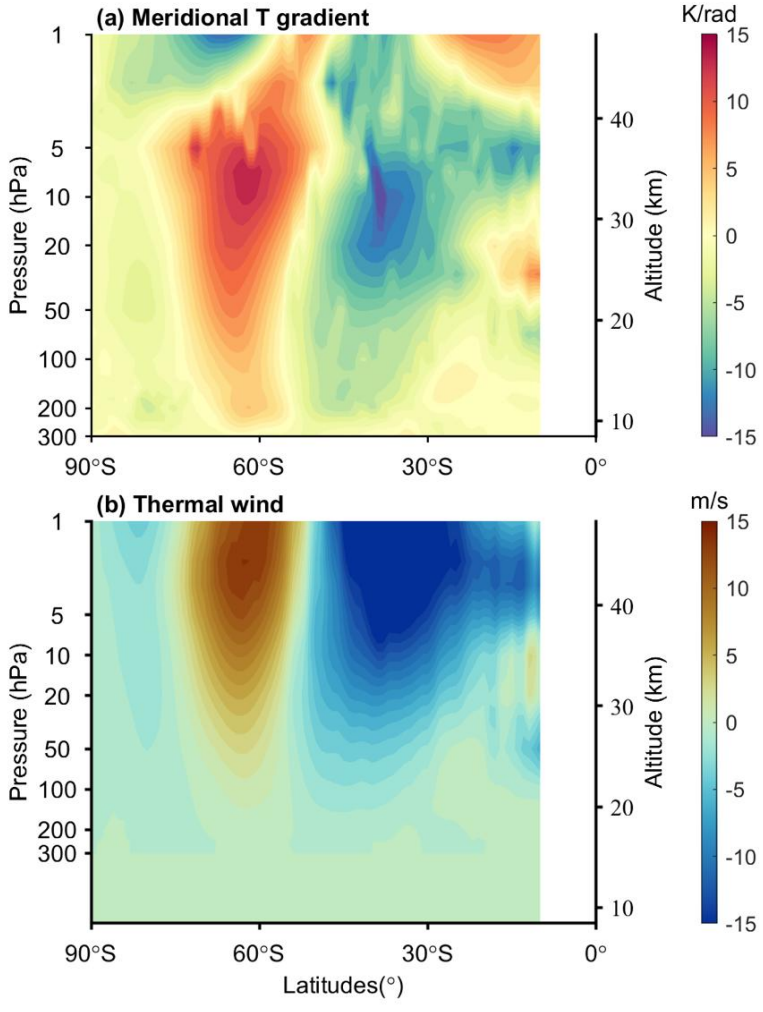

Figure 7: (a) Meridional gradient of temperature anomalies (∂T′/∂φ) during the Southern Hemisphere winter associated with positive MIOD events. (b) Corresponding zonal wind anomalies ($\boldsymbol{u}_T'$) derived from the thermal wind equation.

https://doi.org/10.5194/egusphere-2025-4367
Preprint. Discussion started: 23 September 2025

However, besides the negative zonal-mean zonal wind anomalies over the midlatitudes (30°–50°S) shown in **Fig. 3**, a region of positive anomalies is also present over high latitudes (60°–75°S) near 3 hPa. This high-latitude response may be linked to the dynamical adjustment associated with the midlatitude wind anomalies. Under the quasi-geostrophic and hydrostatic balance approximation, the zonal wind can be approximated by the thermal wind **(Andrews et al., 1987)**, with both the climatological mean temperature (T) and zonal wind (U) satisfying the thermal wind equation. Accordingly, the zonal thermal wind anomaly ($u_T^{'}$) and the meridional gradient of the temperature anomaly ($T^{'}$) satisfy:

$$\frac{\partial u_T^{'}}{\partial z} = -\frac{R}{aHf}\frac{\partial T^{'}}{\partial \varphi}$$

where $f = 2\,\omega\,sin\,\varphi$ is the Coriolis parameter, R is the gas constant for dry air, a is the Earth's radius, and H is the scale height of the atmosphere. This relationship indicates that the meridional gradient of the temperature anomaly ($\partial T^{'}/\partial\varphi$) thermodynamically forces the vertical shear of the zonal wind.

The positive temperature anomaly in the midlatitude stratosphere, centered near 50° S and ~10 hPa (**Fig. 3b**), induces a marked meridional asymmetry in the temperature gradient ($\partial T^{'}/\partial\varphi$) (**Fig. 7a**), with a strong negative gradient band (–11 K rad^{-1}) between 30° S and 50° S and a positive gradient over 50° S–75° S. According to the thermal wind relationship, this gradient structure drives a typical baroclinic response in the zonal thermal wind anomalies $u_T^{'}$ (**Fig. 7b**): the low-latitude negative gradient region forces a –20 m s^{-1} westerly anomaly centered near the stratopause and extending downward to 100 hPa, while the midlatitude positive gradient anomaly generates an eastward wind anomaly of up to +12 m s^{-1} at the stratopause, and the high-latitude negative gradient corresponds to a secondary –3.4 m s^{-1} anomaly. This thermal wind framework explains the dipolar structure of the zonal wind anomalies in **Fig. 3**, including the high-latitude reversal to positive anomalies. The smaller amplitude of the observed anomalies compared to the calculated thermal wind (e.g., +8 vs. +12 m s^{-1} in mid-to-high latitudes) is mainly due to planetary wave breaking, as indicated by the EP flux divergence (~ –2 m s^{-1} d^{-1} at 60° S, 1 hPa), which acts to weaken the thermal-wind-driven response.

Driven by the zonal momentum forcing provided by the divergence of the E–P flux in the low- and mid-latitude stratosphere, the Brewer–Dobson (B–D) circulation is intensified during positive MIOD events. **Fig. 8a** presents the residual mean meridional and vertical winds (v^*, w^*) calculated from the transformed Eulerian mean (TEM) equations (streamlines), along with

https://doi.org/10.5194/egusphere-2025-4367
Preprint. Discussion started: 23 September 2025

495 percentage anomalies of ozone mixing ratio (color shading), with regions failing the 90% confidence test masked in gray.

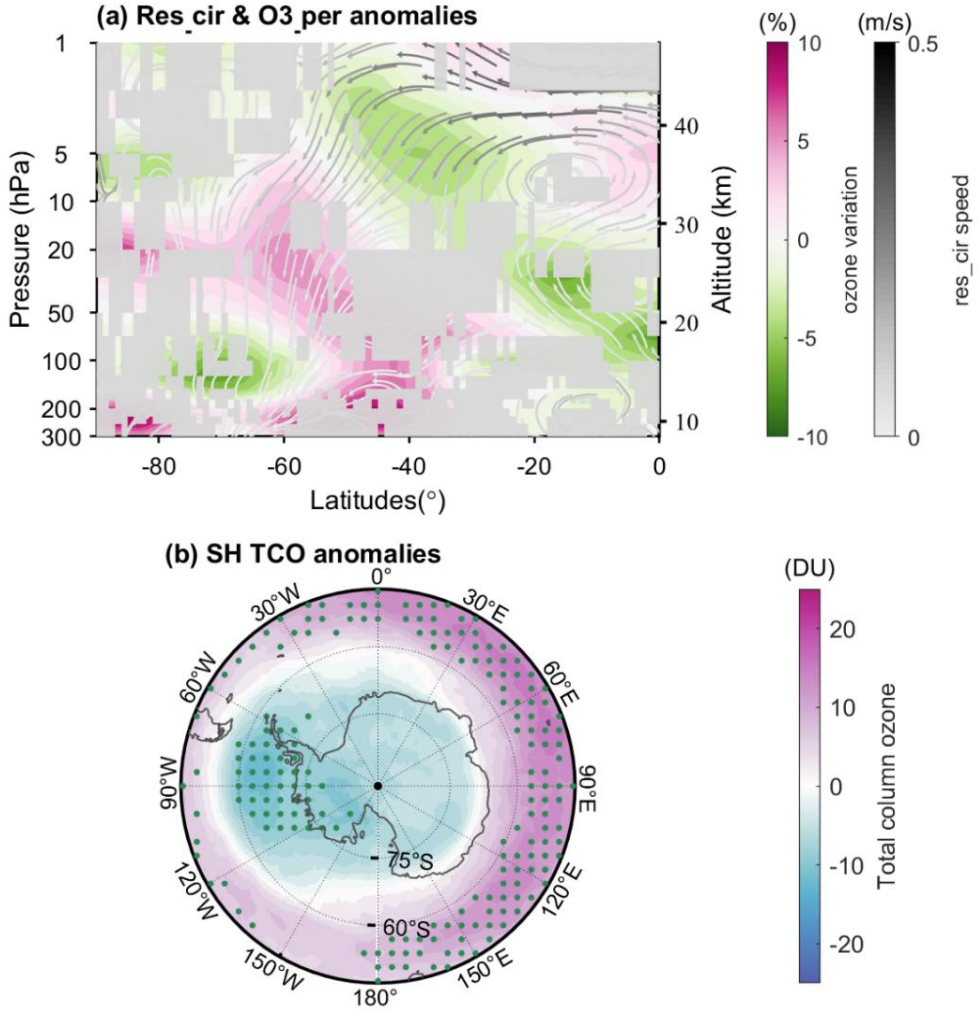

Figure 8: (a) Composite percentage anomalies of ozone mixing ratio relative to the climatological mean and residual circulation anomalies ($\bar{v}^*$, $\bar{w}^*$) during positive MIOD events in June–August (JJA). Shading indicates percentage anomalies of ozone
500 mixing ratio. Streamlines represent anomalies of the residual circulation, with their color indicating the normalized magnitude of the wind anomalies. Gray shading marks regions where the residual circulation anomalies do not pass the 90% Monte Carlo confidence test. (b) Composite anomalies of total column ozone (TCO) during July–August (J–A) for negative MIOD events. Shading indicates composite anomalies of TCO. Stippled areas denote regions that pass the 90% Monte Carlo confidence test.

https://doi.org/10.5194/egusphere-2025-4367
Preprint. Discussion started: 23 September 2025

The results reveal enhanced poleward flow in the stratosphere above 10 hPa between the equator and 40° S, accompanied by strengthened downward motion between 30° and 60° S. In the tropical middle stratosphere (30–40 km), the anomalous ascending branch transports ozone produced by lower-level photochemical reactions upward toward the stratopause, generating a pronounced ozone enhancement (+4 %). Near the stratopause (~3 hPa), the intensified poleward transport in the anomalous circulation produces a marked divergence region in the midlatitudes, leading to ozone depletion of up to –6 %. With increasing latitude, the meridional flow weakens and anomalous subsidence strengthens, forming a convergence center in the mid-stratosphere over the midlatitudes (30 hPa, 60° S), where ozone is accumulated (+6 %) and subsequently heats the atmosphere via shortwave absorption.

This "tropical ascent–midlatitude descent" anomaly pattern redistributes ozone in the latitude–height plane, with the associated changes resulting primarily from transport. It leads to reduced ozone in the tropical lower stratosphere and the midlatitude upper stratosphere, while enhancing ozone in the midlatitude middle–lower stratosphere. As ozone concentrations typically peak near ~20 hPa, changes above 10 hPa-such as the decrease near 40°S and the concurrent tropical increase-indicate substantial anomalies in ozone transport. The increased ozone in the midlatitude stratosphere is likely an important factor contributing to the significant warming over 45°-60°S through radiative heating. However, given the potential influence of Brewer-Dobson circulation anomalies, especially in the lower stratosphere, the exact relative contributions of radiative and dynamical processes cannot be determined from the present analysis. Such ozone transport anomalies are also clearly reflected in the total column ozone (TCO) changes shown in **Fig. 8b**, with a pronounced increase of approximately 20 DU over the midlatitudes (45°–60° S) and a marked decrease at higher latitudes, particularly within the 60° W-120° E sector. These patterns are consistent with the convergence and divergence features of the anomalous circulation evident in **Fig. 8a**.

4 Discussion

The stratospheric wind anomalies documented above are likely to modulate the wave-mean flow interaction, thereby influencing the mesosphere. To assess the full vertical extent of the MIOD influence, we use merged HALOE–SABER temperature observations (10-100 km) for 1991-2022, restricted to 55° S-equator owing to data gaps poleward of 50° S in HALOE and

https://doi.org/10.5194/egusphere-2025-4367
Preprint. Discussion started: 23 September 2025

limited coverage south of 55° S in SABER. **Fig. 9a** shows composite zonal-mean temperature anomalies for positive MIOD events from merged HALOE-SABER observations (1991-2022), and **Fig. 9b** presents the corresponding SD-WACCM6 simulations. Despite observational gaps at high southern latitudes, both datasets reveal the stratospheric signals discussed above and temperature responses extending into the mesosphere.

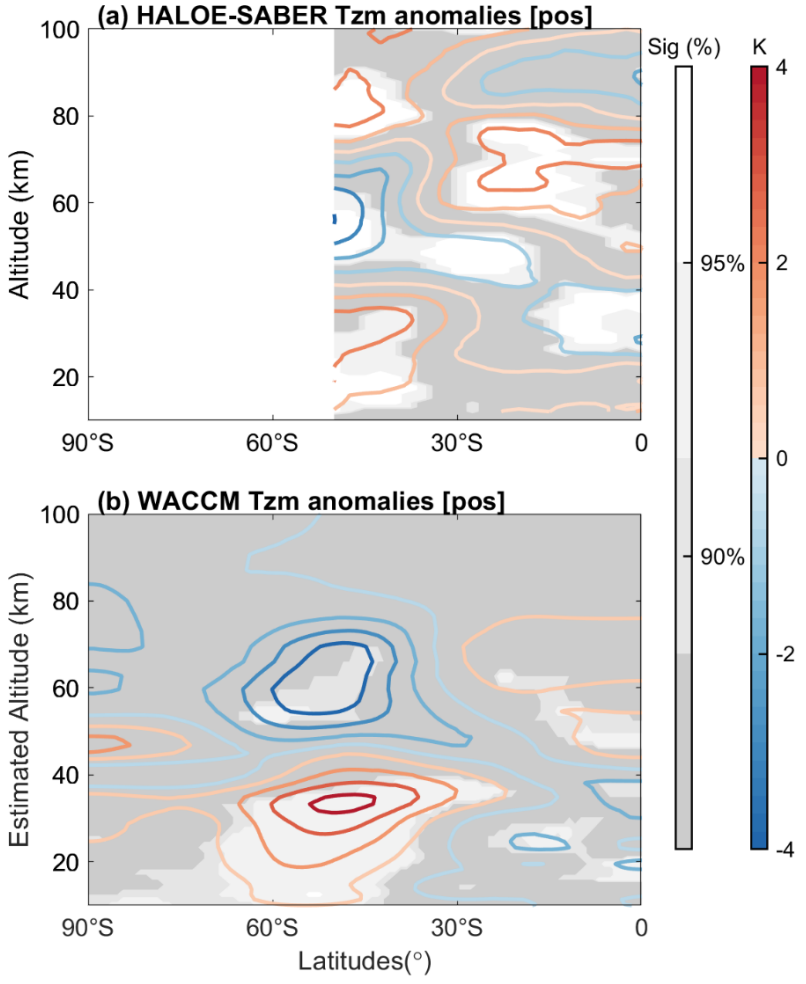

Figure 9: (a) Composite zonal-mean temperature anomalies for positive MIOD events from merged HALOE–SABER satellite observations (1991–2022) over 10–100 km. White, light gray, gray, and dark gray shading denote regions exceeding the 99 %, 95 %, and 90 % confidence levels, and those failing the significance test, respectively, based on a Monte Carlo method. (b) Same as (a), but from SD-WACCM6 simulations.

https://doi.org/10.5194/egusphere-2025-4367
Preprint. Discussion started: 23 September 2025

In the midlatitude stratosphere, satellite observations show zonal-mean temperature anomalies of +3 K at 45° S and 10 hPa, slightly weaker than the +4 K seen in the ERA5 reanalysis. This difference may be due to the satellite data assimilation period (post-1992) not covering earlier strong MIOD events. From the stratopause upward to the mesosphere (1–0.03 hPa), a significant cold anomaly develops, with a –4 K minimum centered at 50° S and a tilted cold band of about –1 K extending from the equatorial stratopause (10 hPa, 0°) toward the lower mesosphere at 30° S (0.3 hPa). Above this level, from the upper mesosphere to the lower thermosphere (0.01-0.001 hPa), the anomalies shift to warming, reaching up to +2 K. From the stratopause to the upper mesosphere (1-0.03 hPa), negative temperature anomalies are observed, with a minimum of –4 K centered over the midlatitudes (50° S) and a tilted cold band (–1 K) extending from the equatorial stratopause (10 hPa, 0°) to the lower mesosphere over 30° S (0.3 hPa). The spatial phase of this cold band closely resembles that of the ozone depletion region (**Fig. 8b**). Above, from the upper mesosphere to the lower thermosphere (0.01-0.001 hPa), the anomalies transition again to warm anomalies of up to +2 K. Observations reveal significant warm anomalies, including a pronounced midlatitude warming in the MLT region and a +1.5 K anomaly near the tropical upper mesosphere (0–30° S, 65–80 km). In contrast, the Specified Dynamics Whole Atmosphere Community Climate Model version 6 (SD-WACCM6) reproduces the overall structure but with weaker amplitudes, where the midlatitude warming is largely absent and the tropical anomaly remains below 1 K and statistically insignificant.

During positive MIOD events, the stratospheric zonal wind anomalies exhibit a distinct dipole pattern, characterized by a pronounced weakening of the midlatitude westerlies ($\Delta u \approx -18$ m s^{-1}). This structure acts as a vertical filter that selectively suppresses gravity wave components propagating in the same direction through critical-level filtering. As a consequence, a strong eastward gravity wave drag anomaly of up to +12 m s^{-1} d^{-1} emerges near 0.1 hPa (80 km) at midlatitudes, driving a secondary westerly wind anomaly (+8 m s^{-1}) above 0.1 hPa around 30° S at 0.01 hPa (**Fig. 10**). At high southern latitudes (60°–80° S), no clear gravity wave drag anomalies are found, and the zonal wind perturbations above 60 km remain weak. This indicates that the influence of positive MIOD events on the middle-to-upper atmosphere is primarily confined to the midlatitudes, while the high-latitude circulation is only marginally affected.

https://doi.org/10.5194/egusphere-2025-4367
Preprint. Discussion started: 23 September 2025

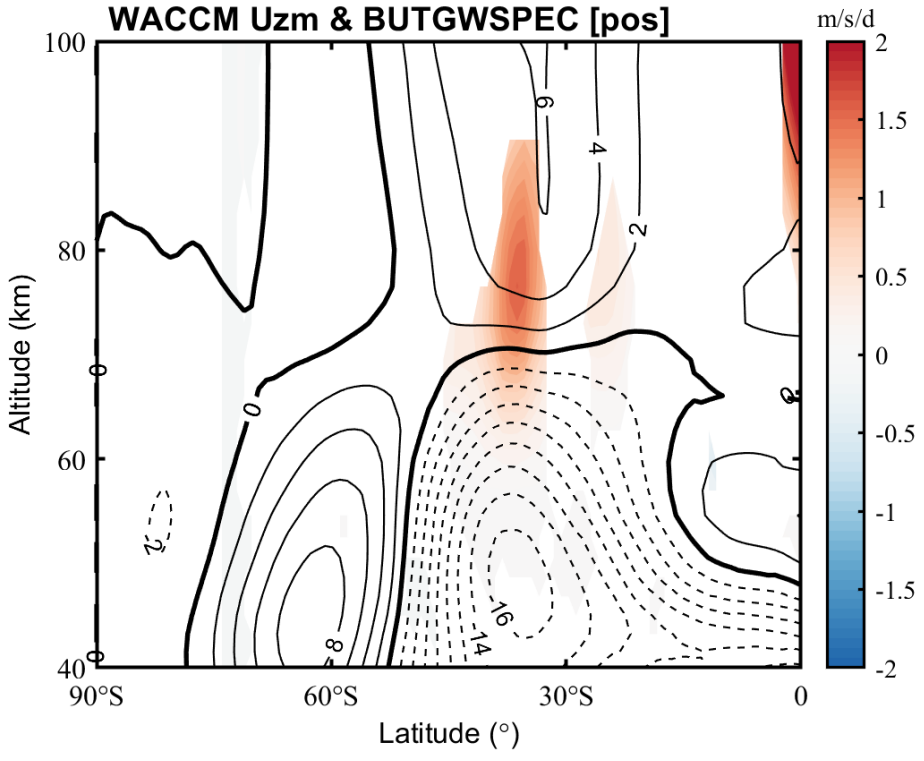

Figure 10: Composite anomalies of JJA zonal mean zonal wind and gravity wave drag in the Southern hemispheric upper stratosphere to the lower thermosphere during positive MIOD events. Contours denote composite anomalies of zonal wind (solid for positive/eastward anomalies and dashed for negative/westward anomalies), with a contour interval of 2 m s^{-1}. Shading indicates anomalies of gravity wave drag, and only regions passing the 90% Monte Carlo confidence test are shown.

The present study demonstrates that the MIOD exerts a substantial influence on the Southern Hemisphere stratosphere and mesosphere. Composite analyses indicate that positive MIOD events are associated with pronounced decelerations of the midlatitude westerlies, enhanced planetary wave propagation, and significant temperature anomalies, whereas negative events generally produce weaker and less coherent responses. This phase asymmetry points to fundamental differences in the underlying dynamical and thermodynamical drivers, consistent with the spatially asymmetric patterns of sea surface temperature anomalies and their ability to modulate planetary wave forcing and background flow interaction. The diagnosed stratospheric anomalies are dynamically consistent with the thermal wind framework, whereby the enhanced

https://doi.org/10.5194/egusphere-2025-4367
Preprint. Discussion started: 23 September 2025

warming near 50° S and ~10 hPa generates strong meridional temperature gradients that are directly linked to the observed dipolar zonal wind anomalies. Discrepancies between thermal-wind estimates and reanalysis winds are largely attributable to planetary wave breaking, as indicated by EP flux divergence, which further provides the momentum forcing that strengthens the Brewer-Dobson circulation, enhancing poleward transport and downward motion in the midlatitudes. This circulation adjustment drives marked ozone redistribution, with enhanced tropical upwelling producing ozone increases near the stratopause, while divergence over the midlatitudes leads to ozone depletion aloft and convergence near 30 hPa and 60° S produces ozone enrichment.

The influence of the MIOD extends into the mesosphere and lower thermosphere (MLT) through gravity-wave filtering modulated by stratospheric wind perturbations. MIOD-related zonal wind anomalies modify the intrinsic phase speeds of gravity waves through Doppler shifting, thereby shifting the altitudes of critical levels. When the background eastward zonal wind weakens, more eastward-propagating gravity waves can pass through the critical levels and reach the mesosphere. This selective filtering process controls the spectrum of upward-propagating waves and the altitudes where they dissipate. The surviving waves break and deposit momentum, producing coherent drag anomalies and mean-flow adjustments that align with the diagnosed wind departures. Enhanced gravity-wave drag centers in the winter midlatitudes near the upper mesosphere (~0.1 hPa) and the associated secondary circulations yield heating and cooling patterns consistent with observed thermal anomalies aloft. The overall picture highlights that the MLT response is not a passive extension of stratospheric variability but the outcome of selective filtering, wave–mean flow interactions, and feedbacks. Small discrepancies in amplitude between observations and SD–WACCM6 simulations likely reflect uncertainties in gravity-wave sources and parameterizations, although the simulated spatial structure and vertical phasing support the proposed mechanism.

The most pronounced responses are linked to positive MIOD events, whereas negative phases produce weaker atmospheric signals. This asymmetry arises from fundamental differences in the accompanying planetary wave activity, with positive events favoring strong wavenumber-1 responses that efficiently transmit the oceanic forcing into the stratosphere, while negative events are associated with weaker or less favorably phased wave activity.

https://doi.org/10.5194/egusphere-2025-4367
Preprint. Discussion started: 23 September 2025

5 Conclusion

The present study highlights the significant role of Southern Hemisphere winter Indian Ocean SST anomalies in modulating the circulation and thermal structure of the middle and upper atmosphere. By constructing a new index based on the leading EOF mode of JJA SST variability, we demonstrate that pronounced planetary wave responses accompany positive SST anomalies, enhanced upward EP flux, and a strengthening of the residual meridional circulation. These dynamical changes favor a warmer polar stratosphere, modifications of the polar vortex morphology, and altered ozone transport pathways. The findings are consistently supported by satellite observations and WACCM6 simulations, lending robustness to the identified SST-atmosphere coupling. Beyond the seasonal mean influence, our results reveal that the SST-driven responses exhibit strong hemispheric asymmetry, with the Southern Hemisphere atmosphere being more sensitive due to its unique background circulation during winter. This sensitivity underlines the importance of considering the Indian Ocean as a key driver of stratospheric variability, in addition to well-known factors such as ENSO and the QBO.

The analysis further suggests that long-term trends in Indian Ocean SST may have contributed to the observed variability in Antarctic ozone depletion and recovery. While ozone forcing has dominated the Southern Hemisphere stratosphere over the past decades, the role of oceanic boundary forcing should not be overlooked, particularly in the context of future climate change when both ozone recovery and continued ocean warming are expected to interact. Taken together, the results emphasize that the Indian Ocean SST anomalies exert a previously underappreciated influence on the Southern Hemisphere middle and upper atmosphere. This coupling mechanism provides new insights into ocean–atmosphere interactions at interannual to decadal timescales. It has implications for predicting the variability of the stratospheric circulation and ozone evolution in a changing climate.

Acknowledgement

This work was supported by the National Natural Science Foundation of China Grants 42130203, 42241115, 42275133, and 42241135, and the National Key R\&D Program of China Grant 2022YFF0503703

https://doi.org/10.5194/egusphere-2025-4367
Preprint. Discussion started: 23 September 2025

Data availability

HALOE satellite observations (1991–2004) are available from the NASA Goddard Earth Sciences Data and Information Services Center (GES DISC) at https://disc.gsfc.nasa.gov/. SABER temperature data (2002–2020) are provided by GATS Inc. and can be accessed via https://saber.gats-inc.com/data.ph. ERA5 reanalysis data are available from the Copernicus Climate Data Store at https://cds.climate.copernicus.eu/. WACCM6 simulations are distributed by the CESM project and can be obtained through the Earth System Grid Federation at https://esgf-node.llnl.gov/projects/esgf-cesm/. The midlatitude Indian Ocean Dipole (MIOD) index constructed in this study is derived from the Hadley Centre Sea Ice and Sea Surface Temperature dataset (HadISST; https://www.metoffice.gov.uk/hadobs/hadisst/). TOMS ozone data are publicly available at https://ozonewatch.gsfc.nasa.gov/meteorology/SH.html. Solar F10.7 flux data are available from NASA's OMNIWeb archive at https://omniweb.gsfc.nasa.gov/. The derived data used for generating the figures displayed in this article are available on **(Yang, 2025)**.

Author contribution

CY, XG, and TL planned the campaign; CY, XG, XW, JZ, and XF performed the measurements; XY, XG, XW, and XF analyzed the data; CY wrote the manuscript draft; TL, XW, JZ, XF, and XX reviewed and edited the manuscript.

References

Andrews, D. G. and McIntyre, M. E.: Planetary Waves in Horizontal and Vertical Shear: The Generalized Eliassen-Palm Relation and the Mean Zonal Acceleration, J. Atmos. Sci., 33, 2031–2048, https://doi.org/10.1175/1520-0469(1976)033<2031:PWIHAV>2.0.CO;2, 1976.

Andrews, D. G., Leovy, C. B., Holton, J. R., Marshall, J., and Plumb, R. A.: Middle Atmosphere Dynamics, Elsevier Science & Technology, Saint Louis, 1987.

Ashok, K., Guan, Z., and Yamagata, T.: Impact of the Indian Ocean dipole on the relationship between the Indian monsoon rainfall and ENSO, Geophysical Research Letters, 28, 4499–4502, https://doi.org/10.1029/2001gl013294, 2001.

Baldwin, M. P. and Dunkerton, T. J.: Stratospheric Harbingers of Anomalous Weather Regimes, Science, 294, 581–584, https://doi.org/10.1126/science.1063315, 2001.

https://doi.org/10.5194/egusphere-2025-4367
Preprint. Discussion started: 23 September 2025

Bègue, N., Bencherif, H., Sivakumar, V., Kirgis, G., Mze, N., and Leclair De Bellevue, J.: Temperature variability and trends in the UT-LS over a subtropical site: Reunion (20.8° S, 55.5° E), Atmos. Chem. Phys., 10, 8563–8574, https://doi.org/10.5194/acp-10-8563-2010, 2010.

Behera, S. K., Salvekar, P. S., and Yamagata, T.: Simulation of Interannual SST Variability in the Tropical Indian Ocean, J. Climate, 13, 3487–3499, https://doi.org/10.1175/1520-0442(2000)013<3487:soisvi>2.0.co;2, 2000.

Black, R. X. and McDaniel, B. A.: Interannual Variability in the Southern Hemisphere Circulation Organized by Stratospheric Final Warming Events, J. Atmos. Sci., 64, 2968–2974, https://doi.org/10.1175/jas3979.1, 2007.

Brayshaw, D. J., Hoskins, B., and Blackburn, M.: The Storm-Track Response to Idealized SST Perturbations in an Aquaplanet GCM, Journal of the Atmospheric Sciences, 65, 2842–2860, https://doi.org/10.1175/2008JAS2657.1, 2008.

Butchart, N., Clough, S. A., Palmer, T. N., and Trevelyan, P. J.: Simulations of an observed stratospheric warming with quasigeostrophic refractive index as a model diagnostic, Quart J Royal Meteoro Soc, 108, 475–502, https://doi.org/10.1002/qj.49710845702, 1982.

Domeisen, D. I. V., Garfinkel, C. I., and Butler, A. H.: The Teleconnection of El Niño Southern Oscillation to the Stratosphere, Rev. Geophys., 57, 5–47, https://doi.org/10.1029/2018RG000596, 2019.

Dowdy, A. J., Vincent, R. A., Murphy, D. J., Tsutsumi, M., Riggin, D. M., and Jarvis, M. J.: The large-scale dynamics of the mesosphere–lower thermosphere during the Southern Hemisphere stratospheric warming of 2002, Geophysical Research Letters, 31, https://doi.org/10.1029/2004gl020282, 2004.

Fletcher, C. G. and Cassou, C.: The Dynamical Influence of Separate Teleconnections from the Pacific and Indian Oceans on the Northern Annular Mode, Journal of Climate, 28, 7985–8002, https://doi.org/10.1175/jcli-d-14-00839.1, 2015.

Fletcher, C. G. and Kushner, P. J.: The Role of Linear Interference in the Annular Mode Response to Tropical SST Forcing, Journal of Climate, 24, 778–794, https://doi.org/10.1175/2010JCLI3735.1, 2011.

García-Herrera, R., Calvo, N., Garcia, R. R., and Giorgetta, M. A.: Propagation of ENSO temperature signals into the middle atmosphere: A comparison of two general circulation models and ERA-40 reanalysis data, J. Geophys. Res., 111, https://doi.org/10.1029/2005jd006061, 2006.

Garfinkel, C. I., Hurwitz, M. M., Oman, L. D., and Waugh, D. W.: Contrasting Effects of Central Pacific and Eastern Pacific El Niño on stratospheric water vapor, Geophysical Research Letters, 40, 4115–4120, https://doi.org/10.1002/grl.50677, 2013.

Garfinkel, C. I., Harari, O., Ziskin Ziv, S., Rao, J., Morgenstern, O., Zeng, G., Tilmes, S., Kinnison, D., O'Connor, F. M., Butchart, N., Deushi, M., Jöckel, P., Pozzer, A., and Davis,

https://doi.org/10.5194/egusphere-2025-4367
Preprint. Discussion started: 23 September 2025

S.: Influence of the El Niño–Southern Oscillation on entry stratospheric water vapor in coupled chemistry–ocean CCMI and CMIP6 models, Atmos. Chem. Phys., 21, 3725–3740, https://doi.org/10.5194/acp-21-3725-2021, 2021.

Gettelman, A., Mills, M. J., Kinnison, D. E., Garcia, R. R., Smith, A. K., Marsh, D. R., Tilmes, S., Vitt, F., Bardeen, C. G., McInerny, J., Liu, H. -L., Solomon, S. C., Polvani, L. M., Emmons, L. K., Lamarque, J. -F., Richter, J. H., Glanville, A. S., Bacmeister, J. T., Phillips, A. S., Neale, R. B., Simpson, I. R., DuVivier, A. K., Hodzic, A., and Randel, W. J.: The Whole Atmosphere Community Climate Model Version 6 (WACCM6), JGR Atmospheres, 124, 12380–12403, https://doi.org/10.1029/2019JD030943, 2019.

Guan, Z. and Yamagata, T.: The unusual summer of 1994 in East Asia: IOD teleconnections, Geophysical Research Letters, 30, https://doi.org/10.1029/2002gl016831, 2003.

Held, I. M., Ting, M., and Wang, H.: Northern Winter Stationary Waves: Theory and Modeling, J. Climate, 15, 2125–2144, https://doi.org/10.1175/1520-0442(2002)015<2125:NWSWTA>2.0.CO;2, 2002.

Hersbach, H., Bell, B., Berrisford, P., Hirahara, S., Horányi, A., Muñoz-Sabater, J., Nicolas, J., Peubey, C., Radu, R., Schepers, D., Simmons, A., Soci, C., Abdalla, S., Abellan, X., Balsamo, G., Bechtold, P., Biavati, G., Bidlot, J., Bonavita, M., De Chiara, G., Dahlgren, P., Dee, D., Diamantakis, M., Dragani, R., Flemming, J., Forbes, R., Fuentes, M., Geer, A., Haimberger, L., Healy, S., Hogan, R. J., Hólm, E., Janisková, M., Keeley, S., Laloyaux, P., Lopez, P., Lupu, C., Radnoti, G., De Rosnay, P., Rozum, I., Vamborg, F., Villaume, S., and Thépaut, J.: The ERA5 global reanalysis, Quart J Royal Meteoro Soc, 146, 1999–2049, https://doi.org/10.1002/qj.3803, 2020.

Joshi, M. M., Charlton, A. J., and Scaife, A. A.: On the influence of stratospheric water vapor changes on the tropospheric circulation, Geophysical Research Letters, 33, https://doi.org/10.1029/2006gl025983, 2006.

Karlsson, B., Randall, C. E., Shepherd, T. G., Harvey, V. L., Lumpe, J., Nielsen, K., Bailey, S. M., Hervig, M., and Russell, J. M.: On the seasonal onset of polar mesospheric clouds and the breakdown of the stratospheric polar vortex in the Southern Hemisphere, J. Geophys. Res., 116, https://doi.org/10.1029/2011jd015989, 2011.

Li, T., Calvo, N., Yue, J., Dou, X., Russell, J. M., Mlynczak, M. G., She, C.-Y., and Xue, X.: Influence of El Niño-Southern Oscillation in the mesosphere: ENSO IN THE MESOSPHERE, Geophys. Res. Lett., 40, 3292–3296, https://doi.org/10.1002/grl.50598, 2013.

Li, T., Calvo, N., Yue, J., Russell, J. M., Smith, A. K., Mlynczak, M. G., Chandran, A., Dou, X., and Liu, A. Z.: Southern Hemisphere Summer Mesopause Responses to El Niño–Southern Oscillation, Journal of Climate, 29, 6319–6328, https://doi.org/10.1175/JCLI-D-15-0816.1, 2016a.

Li, T., Calvo, N., Yue, J., Russell, J. M., Smith, A. K., Mlynczak, M. G., Chandran, A., Dou, X., and Liu, A. Z.: Southern Hemisphere Summer Mesopause Responses to El Niño–Southern

https://doi.org/10.5194/egusphere-2025-4367
Preprint. Discussion started: 23 September 2025

Oscillation, Journal of Climate, 29, 6319–6328, https://doi.org/10.1175/JCLI-D-15-0816.1, 2016b.

Li, T., Yue, J., Russell, J. M., and Zhang, X.: Long-term trend and solar cycle in the middle atmosphere temperature revealed from merged HALOE and SABER datasets, Journal of Atmospheric and Solar-Terrestrial Physics, 212, 105506, https://doi.org/10.1016/j.jastp.2020.105506, 2021.

Limpasuvan, V., Hartmann, D. L., Thompson, D. W. J., Jeev, K., and Yung, Y. L.: Stratosphere-troposphere evolution during polar vortex intensification, J. Geophys. Res., 110, 2005JD006302, https://doi.org/10.1029/2005JD006302, 2005.

Lindzen, R. S.: Turbulence and stress owing to gravity wave and tidal breakdown, J. Geophys. Res., 86, 9707, https://doi.org/10.1029/JC086iC10p09707, 1981.

Maycock, A. C., Joshi, M. M., Shine, K. P., and Scaife, A. A.: The Circulation Response to Idealized Changes in Stratospheric Water Vapor, Journal of Climate, 26, 545–561, https://doi.org/10.1175/jcli-d-12-00155.1, 2013.

Mbatha, N., Sivakumar, V., Malinga, S. B., Bencherif, H., and Pillay, S. R.: Study on the impact of sudden stratosphere warming in the upper mesosphere-lower thermosphere regions using satellite and HF radar measurements, Atmos. Chem. Phys., 10, 3397–3404, https://doi.org/10.5194/acp-10-3397-2010, 2010.

Mitchell, N. J., Middleton, H. R., Beard, A. G., Williams, P. J. S., and Muller, H. G.: The 16-day planetary wave in the mesosphere and lower thermosphere, Ann. Geophys., 17, 1447–1456, https://doi.org/10.1007/s00585-999-1447-9, 1999.

Newman, P. A., Daniel, J. S., Waugh, D. W., and Nash, E. R.: A new formulation of equivalent effective stratospheric chlorine (EESC), Atmos. Chem. Phys., 7, 4537–4552, https://doi.org/10.5194/acp-7-4537-2007, 2007.

Ramsay, H. A., Richman, M. B., and Leslie, L. M.: The Modulating Influence of Indian Ocean Sea Surface Temperatures on Australian Region Seasonal Tropical Cyclone Counts, J. Climate, 30, 4843–4856, https://doi.org/10.1175/jcli-d-16-0631.1, 2017.

Rao, J. and Ren, R.: A decomposition of ENSO's impacts on the northern winter stratosphere: competing effect of SST forcing in the tropical Indian Ocean, Clim Dyn, 46, 3689–3707, https://doi.org/10.1007/s00382-015-2797-5, 2016.

Rao, J. and Ren, R.: Varying stratospheric responses to tropical Atlantic SST forcing from early to late winter, Clim Dyn, 51, 2079–2096, https://doi.org/10.1007/s00382-017-3998-x, 2018.

Rao, J. and Ren, R.: Modeling study of the destructive interference between the tropical Indian Ocean and eastern Pacific in their forcing in the southern winter extratropical stratosphere during ENSO, Clim Dyn, 54, 2249–2266, https://doi.org/10.1007/s00382-019-05111-6, 2020.

https://doi.org/10.5194/egusphere-2025-4367
Preprint. Discussion started: 23 September 2025

Rao, J., Garfinkel, C. I., and White, I. P.: Predicting the Downward and Surface Influence of the February 2018 and January 2019 Sudden Stratospheric Warming Events in Subseasonal to Seasonal (S2S) Models, JGR Atmospheres, 125, https://doi.org/10.1029/2019jd031919, 2020.

Rathore, S., Bindoff, N. L., Phillips, H. E., and Feng, M.: Recent hemispheric asymmetry in global ocean warming induced by climate change and internal variability, Nat Commun, 11, 2008, https://doi.org/10.1038/s41467-020-15754-3, 2020.

Rayner, N. A., Parker, D. E., Horton, E. B., Folland, C. K., Alexander, L. V., Rowell, D. P., Kent, E. C., and Kaplan, A.: Global analyses of sea surface temperature, sea ice, and night marine air temperature since the late nineteenth century, J. Geophys. Res., 108, 2002JD002670, https://doi.org/10.1029/2002JD002670, 2003.

Risbey, J. S., Pook, M. J., McIntosh, P. C., Wheeler, M. C., and Hendon, H. H.: On the Remote Drivers of Rainfall Variability in Australia, Monthly Weather Review, 137, 3233–3253, https://doi.org/10.1175/2009MWR2861.1, 2009.

Russell Iii, J. M., Mlynczak, M. G., Gordley, L. L., Tansock, Jr., J. J., and Esplin, R. W.: Overview of the SABER experiment and preliminary calibration results, SPIE's International Symposium on Optical Science, Engineering, and Instrumentation, Denver, CO, USA, 277, https://doi.org/10.1117/12.366382, 1999.

Russell, J. M., Gordley, L. L., Park, J. H., Drayson, S. R., Hesketh, W. D., Cicerone, R. J., Tuck, A. F., Frederick, J. E., Harries, J. E., and Crutzen, P. J.: The Halogen Occultation Experiment, J. Geophys. Res., 98, 10777–10797, https://doi.org/10.1029/93JD00799, 1993.

Ryan, S., Ummenhofer, C. C., Gawarkiewicz, G., Wagner, P., Scheinert, M., Biastoch, A., and Böning, C. W.: Depth Structure of Ningaloo Niño/Niña Events and Associated Drivers, Journal of Climate, 34, 1767–1788, https://doi.org/10.1175/jcli-d-19-1020.1, 2021.

Saji, N. and Yamagata, T.: Possible impacts of Indian Ocean Dipole mode events on global climate, Clim. Res., 25, 151–169, https://doi.org/10.3354/cr025151, 2003.

Saji, N. H., Goswami, B. N., Vinayachandran, P. N., and Yamagata, T.: A dipole mode in the tropical Indian Ocean, Nature, 401, 360–363, https://doi.org/10.1038/43854, 1999.

Shindell, D. T.: Climate and ozone response to increased stratospheric water vapor, Geophysical Research Letters, 28, 1551–1554, https://doi.org/10.1029/1999gl011197, 2001.

Smith, W. H. F. and Sandwell, D. T.: Global Sea Floor Topography from Satellite Altimetry and Ship Depth Soundings, Science, 277, 1956–1962, https://doi.org/10.1126/science.277.5334.1956, 1997.

Solomon, S., Rosenlof, K. H., Portmann, R. W., Daniel, J. S., Davis, S. M., Sanford, T. J., and Plattner, G.-K.: Contributions of Stratospheric Water Vapor to Decadal Changes in the Rate of Global Warming, Science, 327, 1219–1223, https://doi.org/10.1126/science.1182488, 2010.

https://doi.org/10.5194/egusphere-2025-4367
Preprint. Discussion started: 23 September 2025

Son, S., Purich, A., Hendon, H. H., Kim, B., and Polvani, L. M.: Improved seasonal forecast using ozone hole variability?, Geophysical Research Letters, 40, 6231–6235, https://doi.org/10.1002/2013GL057731, 2013.

Sun, S., Fang, Y., Zu, Y., Liu, L., and Li, K.: Increased occurrences of early Indian Ocean Dipole under global warming, Sci. Adv., 8, eadd6025, https://doi.org/10.1126/sciadv.add6025, 2022.

Swadhin, B. K. and Yamagata, T.: Subtropical SST dipole events in the southern Indian Ocean, Geophysical Research Letters, 28, 327–330, https://doi.org/10.1029/2000gl011451, 2001.

Tandon, N. F., Polvani, L. M., and Davis, S. M.: The Response of the Tropospheric Circulation to Water Vapor–Like Forcings in the Stratosphere, Journal of Climate, 24, 5713–5720, https://doi.org/10.1175/JCLI-D-11-00069.1, 2011.

Tong, B., Zhou, W., and Wang, X.: Rising warm positive Indian Ocean dipole under global warming: Early western Indian Ocean warming as a key predictor, One Earth, 8, 101277, https://doi.org/10.1016/j.oneear.2025.101277, 2025.

Tozuka, T., Endo, S., and Yamagata, T.: Anomalous Walker circulations associated with two flavors of the Indian Ocean Dipole, Geophysical Research Letters, 43, 5378–5384, https://doi.org/10.1002/2016gl068639, 2016.

Van Der A, R. J., Allaart, M. A. F., and Eskes, H. J.: Multi sensor reanalysis of total ozone, Atmos. Chem. Phys., 10, 11277–11294, https://doi.org/10.5194/acp-10-11277-2010, 2010.

Xie, F., Zhou, X., Li, J., Chen, Q., Zhang, J., Li, Y., Ding, R., Xue, J., and Ma, X.: Effect of the Indo-Pacific Warm Pool on Lower-Stratospheric Water Vapor and Comparison with the Effect of ENSO, Journal of Climate, 31, 929–943, https://doi.org/10.1175/JCLI-D-17-0575.1, 2018.

Xie, F., Tian, W., Zhou, X., Zhang, J., Xia, Y., and Lu, J.: Increase in Lower Stratospheric Water Vapor in the Past 100 Years Related to Tropical Atlantic Warming, Geophysical Research Letters, 47, e2020GL090539, https://doi.org/10.1029/2020GL090539, 2020.

Xie, S.-P., Hu, K., Hafner, J., Tokinaga, H., Du, Y., Huang, G., and Sampe, T.: Indian Ocean Capacitor Effect on Indo–Western Pacific Climate during the Summer following El Niño, Journal of Climate, 22, 730–747, https://doi.org/10.1175/2008JCLI2544.1, 2009.

Yang, C.: Impact of the Indian Ocean Sea Surface Temperature on the Southern Hemisphere Middle Atmosphere, https://doi.org/10.5281/ZENODO.17014998, 2025.

Yang, C., Li, T., Dou, X., and Xue, X.: Signal of central Pacific El Niño in the Southern Hemispheric stratosphere during austral spring, JGR Atmospheres, 120, https://doi.org/10.1002/2015JD023486, 2015.

Yang, C., Li, T., Smith, A. K., and Dou, X.: The Response of the Southern Hemisphere Middle Atmosphere to the Madden–Julian Oscillation during Austral Winter Using the Specified-

https://doi.org/10.5194/egusphere-2025-4367
Preprint. Discussion started: 23 September 2025

Dynamics Whole Atmosphere Community Climate Model, Journal of Climate, 30, 8317–
865 8333, https://doi.org/10.1175/JCLI-D-17-0063.1, 2017.

Yang, C., Li, T., Lai, D., Wang, X., Xue, X., and Dou, X.: The Delayed Response of the Troposphere-Stratosphere-Mesosphere Coupling to the 2019 Southern SSW, Geophysical Research Letters, 49, https://doi.org/10.1029/2022gl101759, 2022.